



## Computationally Directed Discovery of MoBi<sub>2</sub>

Item Type	article
Authors	Altman, Alison B.;Tamerius, Alexandra D.;Koocher, Nathan Z.;Meng, Yue;Pickard, Chris J.;Walsh, James P. S.;Rondinelli, James M.;Jacobsen, Steven D.;Freedman, Danna E.
DOI	<a href="https://doi.org/10.1021/jacs.0c09419">10.1021/jacs.0c09419</a>
Rights	UMass Amherst Open Access Policy
Download date	2026-05-17 11:43:04
Item License	<a href="http://creativecommons.org/licenses/by-nc-nd/4.0/">http://creativecommons.org/licenses/by-nc-nd/4.0/</a>
Link to Item	<a href="https://hdl.handle.net/20.500.14394/6646">https://hdl.handle.net/20.500.14394/6646</a>

# Computationally Directed Discovery of $\text{MoBi}_2$

Alison B. Altman, Alexandra D. Tamerius, Nathan Z. Koocher, Yue Meng, Chris J. Pickard,\* James P. S. Walsh,\* James M. Rondinelli,\* Steven D. Jacobsen,\* and Danna E. Freedman\*



Cite This: *J. Am. Chem. Soc.* 2021, 143, 214–222



Read Online

ACCESS |



Metrics & More

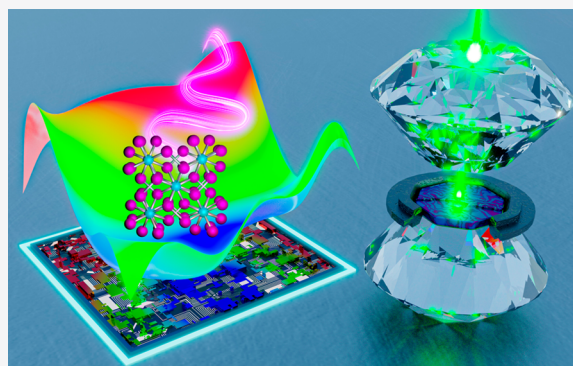


Article Recommendations



Supporting Information

**ABSTRACT:** Incorporating bismuth, the heaviest element stable to radioactive decay, into new materials enables the creation of emergent properties such as permanent magnetism, superconductivity, and nontrivial topology. Understanding the factors that drive Bi reactivity is critical for the realization of these properties. Using pressure as a tunable synthetic vector, we can access unexplored regions of phase space to foster reactivity between elements that do not react under ambient conditions. Furthermore, combining computational and experimental methods for materials discovery at high-pressures provides broader insight into the thermodynamic landscape than can be achieved through experiment alone, informing our understanding of the dominant chemical factors governing structure formation. Herein, we report our combined computational and experimental exploration of the Mo–Bi system, for which no binary intermetallic structures were previously known. Using the ab initio random structure searching (AIRSS) approach, we identified multiple synthetic targets between 0–50 GPa. High-pressure in situ powder X-ray diffraction experiments performed in diamond anvil cells confirmed that Mo–Bi mixtures exhibit rich chemistry upon the application of pressure, including experimental realization of the computationally predicted  $\text{CuAl}_2$ -type  $\text{MoBi}_2$  structure at 35.8(5) GPa. Electronic structure and phonon dispersion calculations on  $\text{MoBi}_2$  revealed a correlation between valence electron count and bonding in high-pressure transition metal–Bi structures as well as identified two dynamically stable ambient pressure polymorphs. Our study demonstrates the power of the combined computational–experimental approach in capturing high-pressure reactivity for efficient materials discovery.



## INTRODUCTION

Extensive exploration of binary phase space has illuminated trends of elemental reactivity and miscibility, quantified temperature- and composition-dependent phase stability, and led to the discovery of thousands of new compounds.<sup>1</sup> Although binary materials are often stoichiometrically simple, generalizable methods for predicting these structures remain elusive because even small changes in chemical composition can give rise to a wide variety of structures.<sup>2</sup> In-depth analysis of known structures has revealed trends in electronic and steric requirements for specific structure types.<sup>3–10</sup> However, the occurrence of “empty” phase space where combinations of elements exhibit no reactivity illustrates significant gaps in our understanding of solid-state structure formation.

The application of pressure provides a tunable parameter for promoting reactivity between elements that do not interact at ambient pressure even at high temperature. Under pressure, multiple chemical factors such as atomic volume, electronic configuration, and orbital occupation become drastically altered from their ambient states.<sup>11–13</sup> Thus, the properties of the elements relative to each other are renormalized, leading to reactions that form materials which appear exotic relative to ambient pressure phases. Notable examples include “simple”

ionic salts that acquire unprecedented oxidation states, the discovery of numerous new metallic hydrides exhibiting record-breaking superconducting critical temperatures, as well as compounds formed by the “inert” noble gases.<sup>14–22</sup> Recent computational efforts have been directed toward codifying these pressure-dependent trends into chemical heuristic scales such as electronegativity, Lewis acidity and chemical hardness that extend across the Periodic Table.<sup>23,24</sup>

The diffuse, metallic bonding exhibited by intermetallic compounds presents a challenge for structure prediction and insight compared to ionically bonded systems. A proven strategy to address this challenge combines computational methods that model the extended electronic structure of intermetallic materials with ab initio structure prediction algorithms that do not rely on known compounds for reference. With sufficiently broad sampling of the high-

Received: September 1, 2020

Published: December 29, 2020



pressure phase space, it becomes possible to map out the phase diagram to direct experimentation. This type of approach is well-suited to predicting binary intermetallic materials, as these structures are often defined by a small number of atoms (<20) related by multiple types of symmetry, resulting in a relatively small phase space of importance.<sup>25</sup> Recently, success has been demonstrated<sup>26</sup> using evolutionary algorithms,<sup>27</sup> simulated annealing or basin-hopping,<sup>28–30</sup> and randomly generated structures.<sup>31,32</sup> The distinct advantage of random structure generation is an essentially unbiased survey of high-pressure phase space.

At ambient pressures, binary Bi compounds display diverse emergent behaviors.<sup>33–35</sup> However, the ambient pressure reactivity of Bi is limited, perhaps due to the extreme chemical softness of this heavy element.<sup>36</sup> This behavior changes significantly with the application of pressure, and the investigation of high-pressure transition metal (TM)–Bi phase space reveals rich chemistry over a range of pressures.<sup>37–40</sup> Notably, thus far no Group 6–Bi binary intermetallic structures have been reported, representing a gap in understanding of how electron counts influence TM–Bi structure. In particular, Group 6 elements present a borderline case in which either the  $ns^2(n-1)d^4$  or  $ns^1(n-1)d^5$  configuration is viable in the isolated atoms, which has implications for their high-pressure electronegativity and reactivity.<sup>24</sup> We hypothesized that using a 4d metal over a 3d metal would promote (meta)stability upon decompression to ambient pressure by reducing the difference in atomic radii and chemical softness. Herein, we describe our combined computational and experimental investigation of pressure-dependent Mo–Bi reactivity.

## RESULTS AND DISCUSSION

**High-Pressure Mo–Bi Structure Prediction.** We began by using the ab initio random structure searching (AIRSS) high-throughput approach (version 0.9.1) to computationally explore high-pressure phase space in search of stable Mo–Bi phases for targeted experimental synthesis.<sup>41</sup> AIRSS integrates with modern density functional theory (DFT) packages to allow for the efficient sampling of potential energy surfaces over vast regions of compositional space using only a minimal level of sensible biasing of randomly generated structures (e.g., minimum separation constraints to prevent atomic core overlap, presence of at least one symmetry element, reasonable starting volumes, etc.).<sup>31,32</sup> Furthermore, because each structure is generated and treated independently, the method is trivially parallelizable to take full advantage of modern computer clusters. In our studies we used CASTEP to relax each of the randomly generated structures toward their nearest energetic minima.<sup>42</sup>

This procedure requires a careful balance between coverage of composition space and sufficiently precise calculated energies. Our preliminary searches were performed using relatively low cutoff energies and soft pseudopotentials to rapidly generate a large number of structures that ensures adequate composition sampling (see the [Supporting Information](#), SI). We ran our first search at 40 GPa, which is near the upper limit of achievable pressure in the specific diamond anvil cell (DAC) employed in our experiments, generating approximately 10 000 relaxed structures. The lowest energy structure was within 25 meV/atom of the elements, demonstrating the enhanced stability of Mo–Bi compounds under high pressures (for reference, in calculations carried out

with the same parameters at 0 GPa, the lowest energy structure had a formation enthalpy of +115 meV/atom).

To gather more accurate energies of the lowest lying structures, and thus better assess their thermodynamic stability, we performed a second round of higher accuracy random structure searches. These calculations are detailed in the SI and involve higher cutoff energies and harder pseudopotentials. The formation enthalpies versus composition for the low-lying ( $\Delta H < 200$  meV) structures are plotted in [Figure 1](#). The

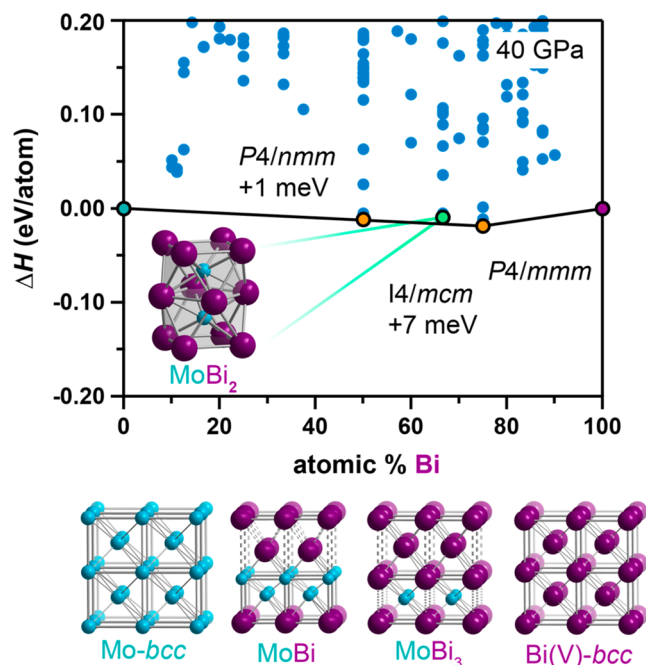


**Figure 1.** Convex hull diagram (top) constructed by comparing the enthalpy of randomly generated Mo–Bi structures found at 40 GPa (blue dots) with the enthalpy of the elements (Mo, turquoise; Bi, purple). The three lowest energy compositions found to be stable relative to the elements are highlighted in green and orange, with the predicted structures for MoBi<sub>2</sub>, MoBi, and MoBi<sub>3</sub> and those of the elements shown (inset and bottom).

convex hull is also plotted and reveals that three compositions are expected to adopt structures with negative formation enthalpies relative to the elements at 40 GPa: MoBi (*P4/nmm*), MoBi<sub>2</sub> (*I4/mcm*), and MoBi<sub>3</sub> (*P4/mmm*).

Analysis of these predicted structures gives insight into possible high-pressure chemistry of Mo–Bi mixtures. Beginning with the most stable structure, MoBi<sub>3</sub> (*P4/mmm*) has a calculated formation enthalpy of  $-19$  meV/atom. The second most stable predicted structure, MoBi (*P4/nmm*), has a formation enthalpy of  $-12$  meV/atom, yet lies slightly above the convex hull ( $+1$  meV/atom) due to the high stability of MoBi<sub>3</sub>. We note a common structural motif shared not only by the lowest energy MoBi and MoBi<sub>3</sub> structures, but by all of the structures with these two compositions that are found to be stable relative to the elements: each can be described as alternating layers of square nets, with each layer translated by half of a unit cell resulting in an A B A B type ordering, similar to the body-centered cubic (bcc) structure type. Each stoichiometry manifests as a different pattern of element identity of each layer (A B A' B' for MoBi and A B' A' B' for MoBi<sub>3</sub>) and also leads to a distortion along the stacking axes to account for the size difference between Mo and Bi (see [Figure](#)

1, bottom). The small differences in energy between the most stable phases at each composition ( $<20$  meV/atom) indicate that we could expect to access multiple of these related compositions at experimentally relevant temperatures. The similarities of these predicted phases to each other and to elemental Mo and Bi(V) suggest a lack of atomic site preference, which could manifest experimentally as a bcc substitutional alloy. Because these calculations describe bulk ordered structures (a manifestation of the constrained unit cell size used in the searches), we could not distinguish between an ordered material and a randomly substituted alloy with these structure predictions. The formation of alloys is driven by similarities in atomic size and electronegativity, which are expected to converge for Mo and Bi at moderate pressures.<sup>43</sup> Alloy formation is also consistent with a previous report of an uncharacterized superconducting Mo–Bi material formed from a 1:3 mixture of the elements at 4 GPa,<sup>44</sup> suggesting a reasonable synthetic target in this phase space.

In addition to these modified bcc structures, we found a MoBi<sub>2</sub> candidate phase at 40 GPa with a formation enthalpy of  $-9$  meV/atom, and a distance from the convex hull of  $+7$  meV/atom (Figure 1, inset). Compared to the MoBi (*P4/nmm*) and MoBi<sub>3</sub> (*P4/mmm*) structures, in which the Bi atoms form square nets, the *I4/mcm* structure consists of columns of Bi square antiprisms with Mo chains running through the center of each column. This structure corresponds to the CuAl<sub>2</sub> structure type, one exhibited by over 200 binary intermetallic compounds, but is distinct from the elemental structures of either Mo or Bi. Accordingly, this MoBi<sub>2</sub> structure is present in multiple databases as the result of varied computationally driven material discovery efforts and is found to have a formation enthalpy of  $>+300$  meV/atom at ambient conditions.<sup>45,46</sup> More generally, Bi does not form materials in this structure type at ambient conditions but does react with Fe above 30 GPa and Mn above 8 GPa to form the analogous FeBi<sub>2</sub> and MnBi<sub>2</sub> structures, respectively.<sup>38,47</sup> Similarly, CrSb<sub>2</sub>, which exhibits a marcasite-type structure at ambient pressure, forms the CuAl<sub>2</sub>-type structure at 5.5 GPa.<sup>48</sup> The significant pressure dependent stabilization of the structure combined with the high-pressure prevalence of analogous Bi and Sb materials suggest that CuAl<sub>2</sub>-type MoBi<sub>2</sub> represents an additional promising target for experimental realization at high-pressure.

To probe how the stabilities of these structures and the overall phase diagram vary as a function of pressure, we broadened the computational searches to include higher and lower pressures. We performed five additional random structure searches over 0–50 GPa in steps of 10 GPa, a pressure range that fully captures our experimental capabilities. A summary of the salient structures found across all six searches is given in Table S7. The result of the structure search at 50 GPa was similar to that carried out at 40 GPa, identifying MoBi<sub>3</sub> (*P4/mmm*) as the most stable predicted structure. Although the AIRSS approach identified multiple candidate structures between 0 and 30 GPa corresponding to local minima on the potential energy surface and potentially metastable materials, no binary structures were predicted to be stable relative to the elements (Figure S9). This is consistent with the reported phase diagram for Mo–Bi, which under ambient pressures demonstrates immiscibility of the elements up to elevated temperatures corresponding to the phase change to a mixed gaseous state.<sup>49</sup> We also employed a routine in AIRSS that performs a linear extrapolation of the enthalpies of

the low-energy structures to higher and lower pressures than the searches were run at (this method is described in ref 32, section 6.4).<sup>32</sup> The extrapolated enthalpies are only an approximation, but they indicate that even more compounds would be expected at pressures above 70 GPa (see SI), making this a promising region of phase space for future exploration.

**Synthesis and Structural Analysis of MoBi<sub>2</sub>.** To target these candidates experimentally, we performed high-pressure experiments in a DAC between 5 and 45 GPa. The transparency of diamond to a wide range of radiation wavelengths allowed us to simultaneously heat samples with a near-infrared laser while monitoring their structure with powder X-ray diffraction (PXRD). We loaded cells with mixtures of elemental Mo and Bi which had been compressed into a thin foil. Laser-cut discs of single crystal magnesium oxide (MgO)<sup>50</sup> were used to insulate the sample from the diamonds, as well as serve as a pressure transmitting medium and the pressure calibrant.<sup>51</sup> All manipulation of samples was performed under an inert atmosphere to prevent the formation of oxides. PXRD data were collected using a two-dimensional detector at beamline 16-ID-B, HPCAT, Advanced Photon Source ( $\lambda = 0.406626$  Å, X-ray fwhm of 5  $\mu\text{m}$ ). This experimental setup allowed for simultaneous sample characterization and laser heating, following the procedure described in the SI.<sup>52</sup>

Throughout the pressure range examined, we observed rich reactivity between Mo and Bi. Between 5 and 30 GPa, we detected the formation of new diffraction rings whose weak intensity coupled with their small number precluded structure refinement methods (Figure S5). While this reactivity may be consistent with the predicted ordered phases derived from bcc structure packing arrangements, further experiments are required to definitively determine the structure formed. In comparison, throughout the 35–45 GPa pressure region, we observed the growth of the same single phase expressing multiple high intensity peaks. An example of the diffraction patterns collected while heating in this range is given in Figure 2. We readily indexed these peaks to the *I4/mcm* space group, and Rietveld refinement confirmed that the new phase was MoBi<sub>2</sub> in the CuAl<sub>2</sub>-type structure (Figure 3), consistent with the predicted structure.

The CuAl<sub>2</sub> structure type has been well-studied, leading to established steric and electronic tolerances.<sup>53,54</sup> Steric considerations are a driving force for the formation of this structure type, requiring an atomic radius ratio that balances stabilizing A–B and B–B interactions with destabilizing A–A interactions (where A represents the element in the Cu (Mo) site and B corresponds the element in the Al (Bi) site).<sup>55</sup> At elevated pressures, the atomic radii of Mo and Bi can be approximated from the experimental lattice parameters of their high-pressure elemental bcc structures, affording radii of 1.3153(2) Å and 1.5407(4) Å for 8-coordinate Mo and Bi, respectively, at 35.8(5) GPa. The ratio of the Mo and Bi radii at this pressure is 0.854, falling well within the range required to stabilize the CuAl<sub>2</sub> structure type (between 0.62 and 1.01).<sup>55</sup> We can also evaluate the high-pressure atomic distances found in the structure by extrapolating from the 8-coordinate Bi radius to the 15-coordinate value of relevance to this structure, 1.6023(4) Å.<sup>56</sup> The Mo–Mo distance along the Mo based chains is more than twice the elemental radius, suggesting little interaction. In comparison, the relatively short Mo–Bi distances in the square antiprisms provide strong evidence for bonding (see Table 1 for structural parameters). This is

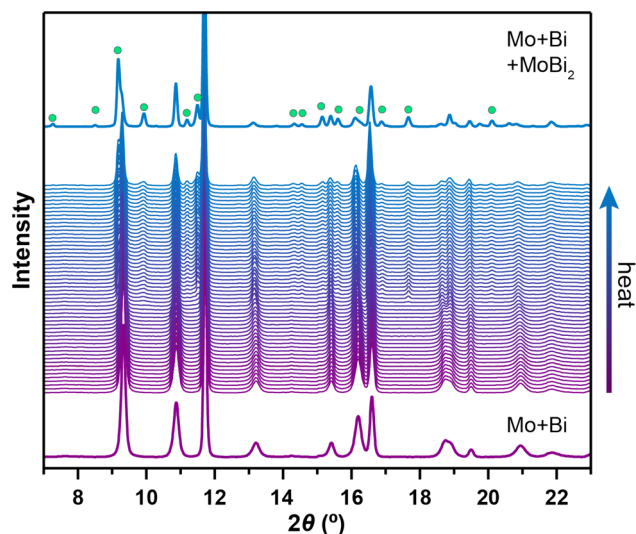


**Figure 2.** In situ PXRD patterns collected while heating a mixture of elemental Mo and Bi at 35.8(5) GPa ( $\lambda = 0.406626 \text{ \AA}$ ) to 1450(5) K. Each pattern has been background subtracted to allow for comparison. At the end of the experiment, we observed peaks corresponding to the MgO insulator, unreacted Bi and Mo as well as new peaks that arose during heating denoted by green dots. The new reflections are consistent with the predicted  $\text{MoBi}_2$  phase.

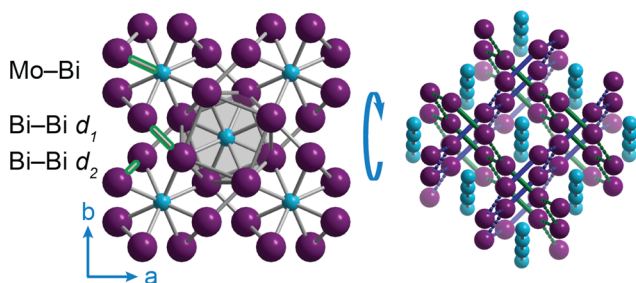


**Figure 3.**  $\text{MoBi}_2$  structure shown from two views (Mo, turquoise; Bi, purple). Viewing along the  $c$ -axis (left) shows the Bi antiprism formed around the chains of Mo atoms, with the shortest Mo–Bi and two shortest Bi–Bi bonds highlighted for clarity. Tilting this structure  $12^\circ$  about the  $a$ -axis (right) provides a view of the distorted interlocking Bi hexagonal networks.

**Table 1. Selected Crystallographic Parameters for the Experimentally Observed  $\text{CuAl}_2$ -type  $\text{MoBi}_2$  Structure**

	$\text{MoBi}_2$ (35.8 GPa)
$a$	6.416(1) $\text{\AA}$
$c$	5.488(3) $\text{\AA}$
$c/a$	0.8554
$x$	0.1529(7)
Mo–Mo	2.744(2) $\text{\AA}$
Mo–Bi	2.793(4) $\text{\AA}$
Bi–Bi ( $d_1$ )	2.774(7) $\text{\AA}$
Bi–Bi ( $d_2$ )	3.261(4) $\text{\AA}$
$d_1/d_2$	0.8507

consistent with the structural picture derived for the high-pressure  $\text{MnBi}_2$  and  $\text{FeBi}_2$  analogues, highlighting that similar high-pressure, high-temperature conditions are required to overcome the immiscibility of Mo and Bi at ambient conditions in order to form a solid-state Mo–Bi bond and a Mo–Bi intermetallic material.<sup>38,47</sup>

Notably, examination of the Bi–Bi interaction in  $\text{MoBi}_2$  revealed significant deviation from the  $\text{CuAl}_2$  structure type. Interlocking hexagonal networks of B (Bi) atoms are crucial to this structure.<sup>53</sup> These require the shortest B (Bi) contact ( $d_1$ ) between atoms on adjacent antiprism columns to roughly equal the second shortest B (Bi) contact ( $d_2$ ) between atoms that form the sides of the triangular faces connecting the upper and lower square faces of each prism. We found that in  $\text{MoBi}_2$  at 35.8(5) GPa  $d_1 = 2.793(6) \text{ \AA}$  and  $d_2 = 3.261(4) \text{ \AA}$ , falling on either side of the threshold for a Bi–Bi bond ( $2r_{\text{Bi}} = 3.2046(8) \text{ \AA}$  at this pressure). This is best quantified by the  $d_1/d_2$  ratio, which falls between 0.85–0.87 over multiple different experiments performed between 35–45 GPa. In comparison, the  $d_1/d_2$  ratios in  $\text{MnBi}_2$  and  $\text{FeBi}_2$  are 0.94 and 0.95, respectively, suggesting  $\text{MoBi}_2$  is more distorted than  $\text{MnBi}_2$  and  $\text{FeBi}_2$ . This motif is rare for this structure type, but has been observed in early transition metal–antimonide analogues, for which  $d_1/d_2 = 0.83, 0.87,$  and  $0.88$  for  $\text{TiSb}_2, \text{V}_{0.96}\text{Sb}_2$  and the high-pressure polymorph of  $\text{CrSb}_2$ , respectively.<sup>48,57,58</sup> Although the difference in principle quantum numbers necessitates caution when comparing  $\text{MoBi}_2$  to these lighter analogues, we hypothesized that a similar distortion mechanism, determined by valence electron count, is operative in the  $\text{MoBi}_2$  structure.

**Electronic Structure of  $\text{MoBi}_2$ .** Given the dearth of Mo–Bi materials and solid-state Mo–Bi bonds, we turned to electronic structure calculations to probe the connection between Bi–Bi distortions in  $\text{MoBi}_2$  and its valence electron count. The short Bi–Bi contacts are readily visualized in the electron localization function (ELF) calculations as discrete dumbbells (Figure 4). While these features suggest a charge separated configuration which may be formally described as  $\text{Mo}^{2+}[\text{Bi}_2]^{2-}$  based on analogous Bi Zintl compounds,<sup>59</sup> the absolute ELF value suggests little localization relative to an electron gas (ELF = 0.5 isosurface shown in Figure 4). Rather than traditional semiconducting Zintl behavior, this reflects the metallic character of the phase consistent with the calculated band structure (Figure S13). Inspection of the electronic projected density of states (PDOS) confirms that the region near the Fermi energy ( $E_{\text{F}}$ ) is dominated by both Bi 6p and Mo 4d electrons. The  $E_{\text{F}}$  falls in a region of high DOS with 2.06 states/eV/f.u., which occurs 1.41 eV above a pseudogap in the DOS. A similar feature is calculated for the  $\text{TiSb}_2$  and  $\text{V}_{0.96}\text{Sb}_2$  members of the subclass of distorted  $\text{CuAl}_2$ -type structures, with an important difference in the position of the Fermi energy relative to the pseudogap.<sup>60</sup> For  $\text{TiSb}_2$ , they coincide, while for  $\text{V}_{0.96}\text{Sb}_2$  the Fermi energy falls above the pseudogap in a region of high DOS. This was previously attributed to the separation of bonding and antibonding states based on weakening of Sb–Sb bonding from  $\text{TiSb}_2$  to  $\text{V}_{0.96}\text{Sb}_2$  determined through Raman spectroscopy experiments. Examination of the crystal orbital Hamilton population (COHP) projection for  $\text{MoBi}_2$  confirms this view applies to this Bi example as well; the bands occupied at  $E_{\text{F}}$  all possess antibonding character, whereas most bonding interactions fall 2–4 eV below  $E_{\text{F}}$ . While differences between Sb and Bi may lead to nuanced effects on the experimentally observed  $d_1/d_2$  ratios with decreasing metal–metal bond strength, we predict an even greater antibonding orbital occupation in  $\text{MoBi}_2$  due to the larger number of valence electrons compared with  $\text{V}_{0.96}\text{Sb}_2$  and  $\text{TiSb}_2$ . We expect this to particularly affect the strong bonds of the pnictogen dumbbells, and conclude that the energy difference between the Fermi energy and the

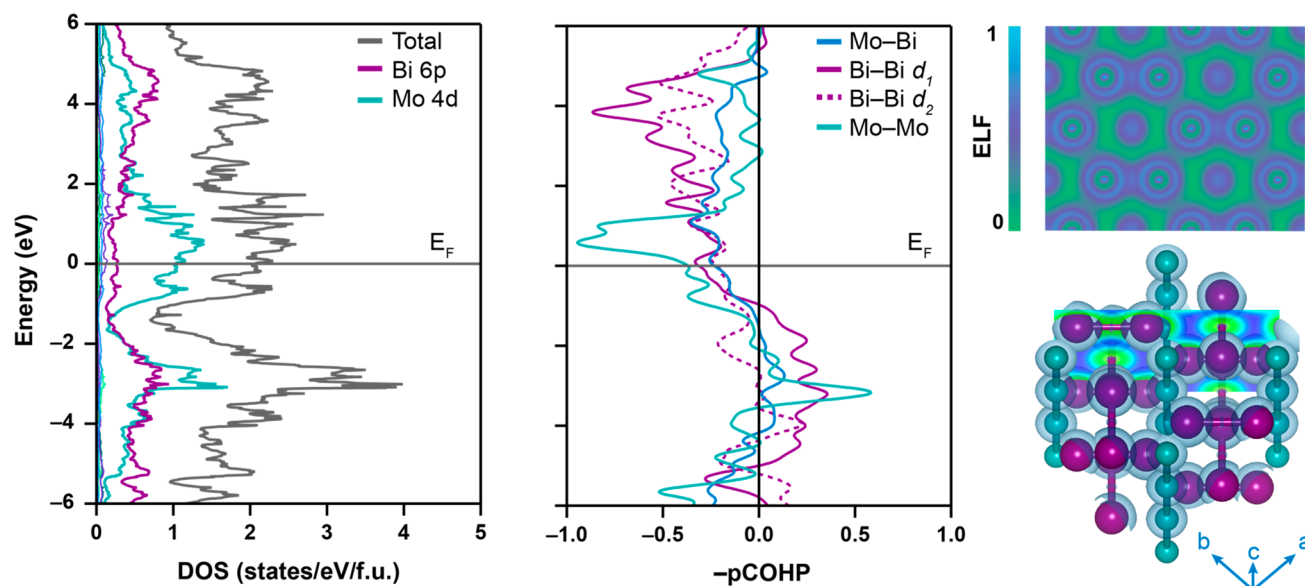


**Figure 4.** Electronic projected density of states (DOS, left), projected crystal Hamiltonian population ( $-pCOHP$ , middle) and isosurface from the electron localization function (ELF, right) of  $MoBi_2$   $I4/mcm$  structure at 40 GPa. The main contribution to the DOS near the Fermi energy derives from the Bi 6p (purple) and Mo 4d (turquoise) orbitals, while the Bi 6s (dark purple), Bi 5d (light blue), Mo 5s (dark green), and Mo 5p (light green) orbitals show minor contributions. The  $pCOHP$  of the atomic pairs with the shortest distances are shown: Mo–Bi (blue), Bi–Bi  $d_1$  (solid purple), Bi–Bi  $d_2$  (dashed purple), and Mo–Mo (turquoise), demonstrating the antibonding character (negative  $-pCOHP$  values) of the valence bands. The ELF isosurface (blue, shown at the 0.5 level, with Bi and Mo depicted as purple and turquoise spheres, respectively) and a section of the ELF parallel to the  $(1\ 1\ 0)$  plane at  $1.5 \times d$  (the lattice-plane spacing) from the origin highlight the Bi–Bi distorted net (right–top) and reveal the presence of Bi–Bi dumbbells.

pseudogap is operative in determining the extent of distortion away from hexagonal networks in these materials.

Similar trends of structural distortions with changing electron counts have been observed in other transition metal-pnictogen systems. In such materials, Hoffmann and co-workers invoked a second-order Jahn–Teller distortion to explain increased structural distortion with greater valence electron count.<sup>61</sup> One may expect that as more valence electrons are added to such structures, there will be a critical point when the energetic gain for the bonding orbitals through a distortion will be offset by the filling of antibonding orbitals and an undistorted structure will again be favored.  $MoBi_2$  falls in the middle of this regime, such that we expect Group 4 and Group 5 analogues to exhibit greater structural distortion, while the  $MnBi_2$  and  $FeBi_2$  analogues exhibit less. However, the electronic structure implications for this trend also imply decreasing stability with increasing electron count due to the occupation of antibonding orbitals for all relevant interactions. This may limit examples of later 4d (TM) $Bi_2$   $CuAl_2$ -type structures while at the same time contextualizing the prediction that the 3d metal analogues are potential ferromagnets undergoing magnetic transitions to relieve the occupation of antibonding orbitals at the Fermi energy.<sup>47,62,63</sup> This highlights the important interplay between structure and electronic properties in these materials.

**Lattice Dynamical Properties of  $MoBi_2$ .** Although we concluded that the valence electron count mainly governs the structural distortions in  $MoBi_2$ , we expected its pressure-dependent properties to be significantly impacted by steric factors. In particular, we were interested in how the inclusion of a larger 4d transition metal affected the dynamic stability of the (TM) $Bi_2$  phase once formed. We therefore performed decompression experiments during which we collected in situ diffraction patterns as we incrementally decreased pressure in

the DAC (Figure S7). Peaks corresponding to  $MoBi_2$  were observed down to  $\sim 3$  GPa. Diffraction patterns collected below this pressure contained  $MgO$ , Mo and the ambient pressure Bi polymorph. While the formation of amorphous materials could not be ruled out, the observed patterns were indicative of the decomposition of  $MoBi_2$  into its constituent elements.

To further explore the Mo–Bi phase space, we computationally analyzed the pressure-dependent structure of the experimental  $I4/mcm$   $MoBi_2$  phase. We began by assessing the Gibbs free energy of formation of the phase. As outlined in the SI, by including a vibrational energy term, we considered entropic contributions to approximate the temperature dependence of its thermodynamic stability. This analysis revealed that  $MoBi_2$  ( $I4/mcm$ ) is only thermodynamically stable over a specific range of pressures and that temperature is an important handle for accessing this phase, consistent with experimentally determined conditions for its synthesis.

Next, we examined the phonon-band dispersions over a series of pressures between 0–40 GPa (Figure 5) to better understand the results of the decompression experiment and the metastability of  $MoBi_2$  in general. Dynamic instability, as seen by imaginary frequency bands in the phonon spectra, reflects the tendency of a structure to undergo a vibrationally driven phase change which could provide insight into the persistence of synthesized phases upon decompression. We found that the relaxed experimental structure is dynamically stable at high-pressures, but at ambient pressure (0 GPa) we observe multiple unstable phonons with imaginary frequencies. Major instabilities arise upon decompression below  $\sim 13$  GPa at the  $\Gamma$  and X points in the Brillouin zone (Figure 5, inset). To assess the effects of these instabilities, we froze these distortions into the structure, which when relaxed yielded a dynamically stable  $MoBi_2$  ( $I4/m$ ) polymorph from the  $\Gamma$  point

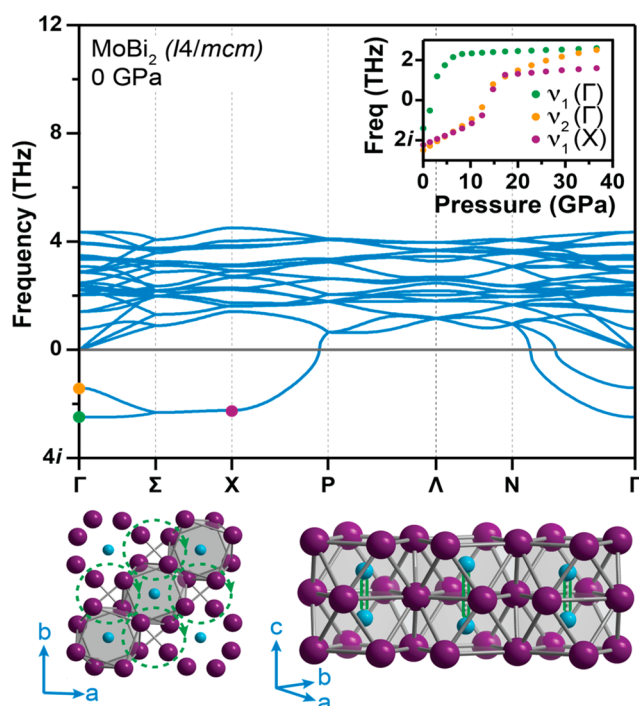


**Figure 5.** Phonon dispersions for  $\text{MoBi}_2$  ( $I4/mcm$ ) at 0 GPa (top) indicate multiple unstable phonons (imaginary frequencies). The pressure dependence of the phonon frequency at the points of interest are shown in the inset ( $\nu_1(\Gamma)$ , green;  $\nu_2(\Gamma)$ , yellow;  $\nu_1(X)$ , purple). Application and subsequent relaxation of the  $\nu_1(\Gamma)$ -distorted structure led to a dynamically stable  $\text{MoBi}_2$  ( $I4/m$ ) polymorph (bottom) with Mo–Mo distortions along the  $c$ -axis (bottom right, denoted by green outline) and rotation of the Bi–Bi dumbbells (bottom left, denoted by dashed green circles).

and a dynamically stable  $\text{MoBi}_2$  ( $Cmcm$ ) polymorph from the X point (Figure 5, green and purple dots, respectively). The ( $I4/m$ ) structure was 13.3 meV/f.u. lower in energy than the ( $Cmcm$ ) phase, so we focus on the ( $I4/m$ ) polymorph in the following discussion (see the SI for details on the ( $Cmcm$ ) phase).

Comparison of the  $\text{MoBi}_2$  polymorphs reveals structural features that underlie the ambient pressure instability of the  $\text{MoBi}_2$  ( $I4/mcm$ ) phase. As shown in Figure 5 (bottom), the distortion driven by the  $\nu_1(\Gamma)$  comprises Peierls-type displacements leading to Mo–Mo dimers that reduce some of the Mo–Mo repulsion as well as rotation of the Bi dumbbells that disrupts the Bi–Bi networks. This creates more space for the larger Bi atoms, potentially allowing for relief of the decreasing  $r_{\text{Mo}}/r_{\text{Bi}}$  ratio which has been implicated in the decomposition of these high-pressure (TM) $\text{Bi}_2$  phases due to breaking of the Mo–Bi and Bi–Bi bonds.<sup>47</sup> Accordingly, we predict a disproportionate lengthening of Mo–Bi and Bi–Bi bonds upon decompression reflecting not just atom expansion but also bond weakening. However, comparison of the integrated pCOHP of the ambient pressure polymorphs suggests that the bonding character of the Mo–Bi bond and the Bi–Bi  $d_2$  interaction increases upon distortion, promoting stabilization (see the SI, Figure S14 and Table S11 for further discussion). While investigation of the thermodynamic stability of the  $\text{MoBi}_2$  ( $I4/m$ ) structure reveals that it does not fall on the convex hull, it is a potential metastable target for synthesis via careful temperature control to allow for kinetic trapping.

## CONCLUSION

The foregoing results illustrate a powerful joint computational and experimental approach to map out and elucidate the chemistry of high-pressure phase space as well as forge a connection with ambient pressure behavior. Through a combination of computational and experimental high-pressure structure searches, we mapped the Mo–Bi binary system. Between 5 and 30 GPa, we observed evidence of the formation of a new compound in low yield, which the results of the AIRSS calculations and literature precedent led us to propose arose from bcc type alloy formation. Driven by similarities in atomic radii and electronegativity with increased pressure, alloy formation may be prevalent throughout high-pressure phase space of larger 4d and 5d TM–Bi mixtures. Above 35 GPa, we discovered the stoichiometric compound  $\text{MoBi}_2$ , the first Group VI–Bi binary intermetallic structure. This represents a significant increase in the diversity of known TM–Bi phases and indicates that the  $\text{CuAl}_2$  structure type is common in high-pressure Bi systems, allowing comparison across analogous (TM) $\text{Bi}_2$  species. This comparison revealed a trend between valence electron count and structure, presenting a viable route toward controlling bonding and electronic properties through variation in TM element identity. The identification of two distorted phases of  $\text{MoBi}_2$  ( $I4/m$  and  $Cmcm$ ) that are dynamically stable at ambient conditions via phonon dispersion calculations indicates our combined computational and experimental approach may also be a promising means for directing the synthesis of mixed metal systems with favorable dynamical properties. Isolation of these materials at ambient conditions will be the focus of future work.

## ASSOCIATED CONTENT

### Supporting Information

The Supporting Information is available free of charge at <https://pubs.acs.org/doi/10.1021/jacs.0c09419>.

Additional synthesis details, crystallographic refinement parameters, and details for AIRSS, electronic structure and phonon dispersion calculations (PDF)

High-pressure crystal structure (CIF)

## AUTHOR INFORMATION

### Corresponding Authors

Chris J. Pickard – Department of Materials Science and Metallurgy, University of Cambridge, Cambridge CB3 0FS, United Kingdom; Advanced Institute for Materials Research, Tohoku University, Aoba, Sendai 980-8577, Japan; Email: [cjp20@cam.ac.uk](mailto:cjp20@cam.ac.uk)

James P. S. Walsh – Department of Chemistry, University of Massachusetts Amherst, Amherst, Massachusetts 01003, United States; [orcid.org/0000-0003-3454-3428](https://orcid.org/0000-0003-3454-3428); Email: [jpswalsh@umass.edu](mailto:jpswalsh@umass.edu)

James M. Rondinelli – Department of Materials Science and Engineering, Northwestern University, Evanston, Illinois 60208, United States; [orcid.org/0000-0003-0508-2175](https://orcid.org/0000-0003-0508-2175); Email: [jrondinelli@northwestern.edu](mailto:jrondinelli@northwestern.edu)

Steven D. Jacobsen – Department of Earth and Planetary Sciences, Northwestern University, Evanston, Illinois 60208, United States; [orcid.org/0000-0002-9746-958X](https://orcid.org/0000-0002-9746-958X); Email: [s-jacobsen@northwestern.edu](mailto:s-jacobsen@northwestern.edu)

Danna E. Freedman – Department of Chemistry, Northwestern University, Evanston, Illinois 60208, United States

States; [orcid.org/0000-0002-2579-8835](https://orcid.org/0000-0002-2579-8835);

Email: [danna.freedman@northwestern.edu](mailto:danna.freedman@northwestern.edu)

## Authors

**Alison B. Altman** – Department of Chemistry, Northwestern University, Evanston, Illinois 60208, United States;

[orcid.org/0000-0002-4975-5004](https://orcid.org/0000-0002-4975-5004)

**Alexandra D. Tamerius** – Department of Chemistry, Northwestern University, Evanston, Illinois 60208, United States

**Nathan Z. Koocher** – Department of Materials Science and Engineering, Northwestern University, Evanston, Illinois 60208, United States

**Yue Meng** – HPCAT, X-Ray Science Division, Argonne National Laboratory, Argonne, Illinois 60439, United States

Complete contact information is available at:

<https://pubs.acs.org/10.1021/jacs.0c09419>

## Notes

The authors declare no competing financial interest.

## ACKNOWLEDGMENTS

We gratefully acknowledge Dr. Michael K. Wojnar, Dr. David Z. Zee, Dr. Danilo Puggioni, and Eric A. Riesel for helpful discussions, Dr. Curtis Kenny-Benson for technical support, and Dr. Chung-Jui Yu for assistance with the table of contents graphic. Experimental work was supported with funding from AFOSR in the form of a PECASE (Grant No. FA9550-17-1-0247). The collaborative project between D.E.F. and S.D.J. was initiated by Northwestern University (NU) through the Innovative Initiatives Incubator (I3), which also partially supported J.P.S.W. Additionally, S.D.J. acknowledges support from the NSF (Grant No. DMR-1508577), and beamtime provided through the Chicago/DOE Alliance Center. A.B.A. acknowledges support from the IIN Postdoctoral Fellowship and the Northwestern University International Institute of Nanotechnology. N.K.Z. and J.M.R. acknowledge the National Science Foundation's MRSEC program (DMR-1720139) at the Materials Research Center of Northwestern University. C.J.P. is supported by the Royal Society through a Royal Society Wolfson Research Merit Award and the EPSRC through Grant No. EP/P022596/1. This work was performed at HPCAT (Sector 16), Advanced Photon Source (APS), Argonne National Laboratory. HPCAT operations are supported by DOE-NNSA's Office of Experimental Sciences. The Advanced Photon Source is a U.S. Department of Energy (DOE) Office of Science User Facility operated for the DOE Office of Science by Argonne National Laboratory under Contract No. DE-AC02-06CH11357. This research was supported in part through the computational resources and staff contributions provided for the Quest high-performance computing facility at Northwestern University which is jointly supported by the Office of the Provost, the Office for Research and Northwestern University Information Technology. This work also made use of the IMSERC the Soft and Hybrid Nanotechnology Experimental (SHyNE) Resource (NSF ECCS-1542205) and Northwestern University as well as the EPIC facility of Northwestern University's NUANCE Center, which has received support from the SHyNE Resource, the IIN, and Northwestern's MRSEC program (NSF DMR-1720139).

## REFERENCES

- (1) Okamoto, H. *Phase Diagrams for Binary Alloys*, 2nd ed.; ASM International: Materials Park, OH, 2010.
- (2) Steurer, W.; Dshemuchadse, J. *Intermetallics: Structures, Properties, and Statistics*; Oxford University Press: Oxford, UK, 2016.
- (3) Villars, P. A Three-Dimensional Structural Stability Diagram for 998 Binary AB Intermetallic Compounds. *J. Less-Common Met.* **1983**, *92*, 215–238.
- (4) Hughbanks, T.; Hoffmann, R. Molybdenum Chalcogenides: Clusters, Chains, and Extended Solids. The Approach to Bonding in Three Dimensions. *J. Am. Chem. Soc.* **1983**, *105*, 1150–1162.
- (5) Hoffmann, R.; Zheng, C. Making and Breaking Bonds in the Solid State: the ThCr<sub>2</sub>Si<sub>2</sub> Structure. *J. Phys. Chem.* **1985**, *89*, 4175–4181.
- (6) Zheng, C.; Hoffmann, R. An Unusual Electron Count and Electron-Deficient Multi-Center Bonding in One Class of Intermetallics: the BaAl<sub>4</sub>, CaAl<sub>2</sub>Zn<sub>2</sub>, CeMg<sub>2</sub>Si<sub>2</sub> and FCC Al Structures. *Z. Naturforsch., B: J. Chem. Sci.* **1986**, *41b*, 292–320.
- (7) Pettifor, D. G. Structure Maps in Magnetic Alloy Design. *Physica B+C* **1988**, *149*, 3–10.
- (8) Lidin, S.; Larsson, A. K. A Survey of Superstructures in Intermetallic NiAs-Ni<sub>2</sub>In-Type Phases. *J. Solid State Chem.* **1995**, *118*, 313–322.
- (9) Fredrickson, D. C. Parallels in Structural Chemistry Between the Molecular and Metallic Realms Revealed by Complex Intermetallic Phases. *Acc. Chem. Res.* **2018**, *51*, 248–257.
- (10) Mitchell Warden, H. E.; Fredrickson, D. C. Frustrated and Allowed Structural Transitions: the Theory-Guided Discovery of the Modulated Structure of IrSi. *J. Am. Chem. Soc.* **2019**, *141*, 19424–19435.
- (11) Gschneidner, K. A. Physical Properties and Interrelationships of Metallic and Semimetallic Elements. *Solid State Phys.* **1964**, *16*, 275–426.
- (12) Vohra, Y. K.; Spencer, P. T. Novel  $\Gamma$ -Phase of Titanium Metal at Megabar Pressures. *Phys. Rev. Lett.* **2001**, *86*, 3068–3071.
- (13) Degtyareva, V. F. Potassium Under Pressure: Electronic Origin of Complex Structures. *Solid State Sci.* **2014**, *36*, 62–72.
- (14) Zhang, W.; Oganov, A. R.; Goncharov, A. F.; Zhu, Q.; Boulfelfel, S. E.; Lyakhov, A. O.; Stavrou, E.; Somayazulu, M.; Prakapenka, V. B.; Konopkova, Z. Unexpected Stable Stoichiometries of Sodium Chlorides. *Science* **2013**, *342*, 1502–1505.
- (15) Luo, D.; Wang, Y.; Yang, G.; Ma, Y. Barium in High Oxidation States in Pressure-Stabilized Barium Fluorides. *J. Phys. Chem. C* **2018**, *122*, 12448–12453.
- (16) Matsuoka, T.; Hishida, M.; Kuno, K.; Hirao, N.; Ohishi, Y.; Sasaki, S.; Takahama, K.; Shimizu, K. Superconductivity of Platinum Hydride. *Phys. Rev. B: Condens. Matter Mater. Phys.* **2019**, *99*, 144511–144516.
- (17) Salke, N. P.; Davari Esfahani, M. M.; Yedukondalu, N.; Zhang, Y.; Kruglov, I. A.; Zhou, J.; Greenberg, E.; Prakapenka, V. B.; Liu, J.; Oganov, A. R.; Lin, J.-F. Prediction and Synthesis of Dysprosium Hydride Phases at High Pressure. *Inorg. Chem.* **2020**, *59*, 5303–5312.
- (18) Salke, N. P.; Davari Esfahani, M. M.; Zhang, Y.; Kruglov, I. A.; Zhou, J.; Wang, Y.; Greenberg, E.; Prakapenka, V. B.; Liu, J.; Oganov, A. R.; Lin, J.-F. Synthesis of Clathrate Cerium Superhydride CeH<sub>9</sub> At 80–100 GPa with Atomic Hydrogen Sublattice. *Nat. Commun.* **2019**, *10*, 764–10.
- (19) Dong, X.; Oganov, A. R.; Goncharov, A. F.; Stavrou, E.; Lobanov, S.; Saleh, G.; Qian, G.-R.; Zhu, Q.; Gatti, C.; Deringer, V. L.; Dronskowski, R.; Zhou, X.-F.; Prakapenka, V. B.; Konopkova, Z.; Popov, I. A.; Boldyrev, A. I.; Wang, H.-T. A Stable Compound of Helium and Sodium at High Pressure. *Nat. Chem.* **2017**, *9*, 440–445.
- (20) Liu, H.; Naumov, I. I.; Hoffmann, R.; Ashcroft, N. W.; Hemley, R. J. Potential High-Tc superconducting Lanthanum and Yttrium Hydrides at High Pressure. *Proc. Natl. Acad. Sci. U. S. A.* **2017**, *114*, 6990–6995.
- (21) Somayazulu, M.; Ahart, M.; Mishra, A. K.; Geballe, Z. M.; Baldini, M.; Meng, Y.; Struzhkin, V. V.; Hemley, R. J. Evidence for

Superconductivity Above 260 K in Lanthanum Superhydride at Megabar Pressures. *Phys. Rev. Lett.* **2019**, *122*, 1–6.

(22) Drozdov, A. P.; Kong, P. P.; Minkov, V. S.; Besedin, S. P.; Kuzovnikov, M. A.; Mozaffari, S.; Balicas, L.; Balakirev, F. F.; Graf, D. E.; Prakapenka, V. B.; Greenberg, E.; Knyazev, D. A.; Tkacz, M.; Eremets, M. I. Superconductivity at 250 K in Lanthanum Hydride Under High Pressures. *Nature* **2019**, *569*, 528–531.

(23) Dong, X.; Oganov, A. R.; Qian, G.; Zhou, X.-F.; Zhu, Q.; Wang, H.-T. How Do Chemical Properties of the Atoms Change Under Pressure? *arXiv (Materials Science)*, March 1, **2015**, ver. 1.

(24) Rahm, M.; Cammi, R.; Ashcroft, N. W.; Hoffmann, R. Squeezing All Elements in the Periodic Table: Electron Configuration and Electronegativity of the Atoms Under Compression. *J. Am. Chem. Soc.* **2019**, *141*, 10253–10271.

(25) Zurek, E. The Pressing Role of Theory in Studies of Compressed Matter. In *Handbook of Solid State Chemistry*; Wiley-VCH: Weinheim, Germany, 2017; pp 571–605.

(26) Oganov, A. R.; Pickard, C. J.; Zhu, Q.; Needs, R. J. Structure Prediction Drives Materials Discovery. *Nat. Rev. Mater.* **2019**, *4*, 331–348.

(27) Oganov, A. R.; Oganov, Ma, Y.; Lyakhov, A. O.; Valle, M.; Gattic, C. Evolutionary Crystal Structure Prediction and Novel High-Pressure Phases. In *High-Pressure Crystallography. NATO Science for Peace and Security Series B Physics and Biophysics*; Boldyreva, E., Dera, P., Eds.; Springer: Dordrecht, 2010.

(28) Kirkpatrick, S.; Gelatt, C. D.; Vecchi, M. P. Optimization by Simulated Annealing. *Science* **1983**, *220*, 671–680.

(29) Goedecker, S. Minima Hopping: an Efficient Search Method for the Global Minimum of the Potential Energy Surface of Complex Molecular Systems. *J. Chem. Phys.* **2004**, *120*, 9911–9917.

(30) Wang, Y.; Ma, Y. Perspective: Crystal Structure Prediction at High Pressures. *J. Chem. Phys.* **2014**, *140*, 040901–040912.

(31) Pickard, C. J.; Needs, R. J. High-Pressure Phases of Silane. *Phys. Rev. Lett.* **2006**, *97*, 045504–045504.

(32) Pickard, C. J.; Needs, R. J. Ab Initio Random Structure Searching. *J. Phys.: Condens. Matter* **2011**, *23*, 053201–053224.

(33) Adams, E.; Hubbard, W. M.; Syeles, A. M. A New Permanent Magnet From Powdered Manganese Bismuthide. *J. Appl. Phys.* **1952**, *23*, 1207–1211.

(34) Alekseevskii, N. E.; Brandt, N. B.; Kostina, T. I. Superconductivity of Binary Alloys of Bismuth. *Bull. Acad. Sci. USSR* **1952**, *16*, 233–263.

(35) Liu, Z. K.; Zhou, B.; Zhang, Y.; Wang, Z. J.; Weng, H. M.; Prabhakaran, D.; Mo, S. K.; Shen, Z. X.; Fang, Z.; Dai, X.; Hussain, Z.; Chen, Y. L. Discovery of a Three-Dimensional Topological Dirac Semimetal,  $\text{Na}_3\text{Bi}$ . *Science* **2014**, *343*, 864–867.

(36) Pearson, R. G. Hard and Soft Acids and Bases. *J. Am. Chem. Soc.* **1963**, *85*, 3533–3539.

(37) Clarke, S. M.; Amsler, M.; Walsh, J. P. S.; Yu, T.; Wang, Y.; Meng, Y.; Jacobsen, S. D.; Wolverton, C.; Freedman, D. E. Creating Binary Cu-Bi Compounds via High-Pressure Synthesis: a Combined Experimental and Theoretical Study. *Chem. Mater.* **2017**, *29*, 5276–5285.

(38) Walsh, J. P. S.; Clarke, S. M.; Meng, Y.; Jacobsen, S. D.; Freedman, D. E. Discovery of  $\text{FeBi}_2$ . *ACS Cent. Sci.* **2016**, *2*, 867–871.

(39) Tencé, S.; Janson, O.; Krellner, C.; Rosner, H.; Schwarz, U.; Grin, Y.; Steglich, F.  $\text{CoBi}_3$ -the First Binary Compound of Cobalt with Bismuth: High-Pressure Synthesis and Superconductivity. *J. Phys.: Condens. Matter* **2014**, *26*, 395701–395707.

(40) Killpatrick, D. H. Pressure-Temperature Phase Diagrams for  $\text{Nb}_3\text{In}$  and  $\text{Nb}_3\text{Bi}$ . *J. Phys. Chem. Solids* **1964**, *25*, 1213–1216.

(41) *Ab Initio Random Structure Searching (AIRSS)*. <https://www.mtg.msm.cam.ac.uk/Codes/AIRSS>.

(42) Clark, S. J.; Segall, M. D.; Pickard, C. J.; Hasnip, P. J.; Probert, M. I. J.; Refson, K.; Payne, M. C. First Principles Methods Using CASTEP. *Z. Kristallogr. - Cryst. Mater.* **2005**, *220*, 567–570.

(43) Zeng, Q.-S.; Ding, Y.; Mao, W. L.; Luo, W.; Blomqvist, A.; Ahuja, R.; Yang, W.; Shu, J.; Sinogeikin, S. V.; Meng, Y.; Brewé, D. L.;

Jiang, J.-Z.; Mao, H. K. Substitutional Alloy of Ce and Al. *Proc. Natl. Acad. Sci. U. S. A.* **2009**, *106*, 2515–2518.

(44) Matthias, B. T.; Jayaraman, A.; Geballe, T. H.; Andres, K.; Corenzwit, E. Many More Superconducting Bismuth Phases. *Phys. Rev. Lett.* **1966**, *17*, 640–643.

(45) Saal, J. E.; Kirklin, S.; Aykol, M.; Meredig, B.; Wolverton, C. Materials Design and Discovery with High-Throughput Density Functional Theory: the Open Quantum Materials Database (OQMD). *JOM* **2013**, *65*, 1501–1509.

(46) Toher, C.; Oses, C.; Hicks, D.; Gossett, E.; Rose, F.; Nath, P.; Usanmaz, D.; Ford, D. C.; Perim, E.; Calderon, C. E.; Plata, J. J.; Lederer, Y.; Jahnátek, M.; Setyawan, W.; Wang, S.; Xue, J.; Rasch, K.; Chepulskii, R. V.; Taylor, R. H.; Gomez, G.; Shi, H.; Supka, A. R.; Rahal Al Orabi Al, R.; Gopal, P.; Cerasoli, F. T.; Liyanage, L.; Wang, H.; Siloi, I.; Agapito, L. A.; Nyshadham, C.; Hart, G. L. W.; Carrete, J.; Legrain, F.; Mingo, N.; Zurek, E.; Isayev, O.; Tropsha, A.; Sanvito, S.; Hanson, R. M.; Takeuchi, I.; Mehl, M. J.; Kolmogorov, A. N.; Yang, K.; D'Amico, P.; Calzolari, A.; Costa, M.; De Gennaro, R.; Nardelli, M. B.; Fornari, M.; Levy, O.; Curtarolo, S.; Cormac. The AFLOW Fleet for Materials Discovery. In *Handbook of Materials Modeling; Methods: Theory and Modeling*; Springer, Cham: Cham, 2020; Vol. 88, pp 1785–1812.

(47) Walsh, J.; Clarke, S. M.; Puggioni, D.; Tamerius, A. D.; Meng, Y.; Rondinelli, J. M.; Jacobsen, S. D.; Freedman, D. E.  $\text{MnBi}_2$ : A Metastable High-Pressure Phase in the Mn-Bi System. *Chem. Mater.* **2019**, *31*, 3083–3088.

(48) Takizawa, H.; Uheda, K.; Endo, T. A New Ferromagnetic Polymorph of  $\text{CrSb}_2$  Synthesized Under High Pressure. *J. Alloys Compd.* **1999**, *287*, 145–149.

(49) Okamoto, H. Bi-Mo (Bismuth-Molybdenum). In *Binary Alloy Phase Diagrams*; Massalski, T. B., Ed.; ASM International: Materials Park, OH, 1990; Vol. 1, pp 762–763.

(50) Hrubciak, R.; Sinogeikin, S.; Rod, E.; Shen, G. The Laser Micro-Machining System for Diamond Anvil Cell Experiments and General Precision Machining Applications at the High Pressure Collaborative Access Team. *Rev. Sci. Instrum.* **2015**, *86*, 072202–072211.

(51) Speziale, S.; Zha, C.-S.; Duffy, T. S.; Hemley, R. J.; Mao, H. K. Quasi-Hydrostatic Compression of Magnesium Oxide to 52 GPa: Implications for the Pressure-Volume-Temperature Equation of State. *J. Geophys. Res.* **2001**, *106*, 515–528.

(52) Meng, Y.; Hrubciak, R.; Rod, E.; Boehler, R.; Shen, G. New Developments in Laser-Heated Diamond Anvil Cell with in Situ Synchrotron X-Ray Diffraction at High Pressure Collaborative Access Team. *Rev. Sci. Instrum.* **2015**, *86*, 072201–072208.

(53) Havinga, E. E.; Damsma, H.; Hokkeling, P. Compounds and Pseudo-Binary Alloys with the  $\text{CuAl}_2(\text{C16})$ -Type Structure I. Preparation and X-Ray Results. *J. Less-Common Met.* **1972**, *27*, 169–186.

(54) Grin, Y.; Wagner, F. R.; Armbruster, M.; Kohout, M.; Leithe-Jasper, A.; Schwarz, U.; Wedig, U.; Georg von Schnering, H.  $\text{CuAl}_2$  Revisited: Composition, Crystal Structure, Chemical Bonding, Compressibility and Raman Spectroscopy. *J. Solid State Chem.* **2006**, *179*, 1707–1719.

(55) Havinga, E. E.; Damsma, H. Compounds and Pseudo-Binary Alloys with the  $\text{CuAl}_2(\text{C16})$ -Type Structure III. Stability and Competitive Structures. *J. Less-Common Met.* **1972**, *27*, 269–280.

(56) Laves, F. *Theory of Alloy Phases*; American Society for Metals: Cleveland, OH, 1956.

(57) Nowotny, H.; Funk, R.; Pesl, J. Kristallchemische Untersuchungen in Den Systemen Mn-As, V-Sb, Ti-Sb. *Monatsh. Chem.* **1951**, *82*, 513–525.

(58) Armbruster, M.; Cardoso Gil, R.; Burkhardt, U.; Grin, Y. Refinement of the Crystal Structures of Titanium Diantimonide,  $\text{TiSb}_2$ , and Vanadium Diantimonide,  $\text{V}_{0.96}\text{Sb}_2$ . *Z. Kristallogr. - New Cryst. Struct.* **2004**, *219*, 229–230.

(59) Dai, D.; Whangbo, M.-H.; Ugrinov, A.; Sevov, S. C.; Wang, F.; Li, L.; Villesuzanne, A.; Alekseyev, A. B.; Liebermann, H.-P.; Buenker, R. J. Analysis of the Effect of Spin-Orbit Coupling on the Electronic Structure and Excitation Spectrum of the  $\text{Bi}_2^{2-}$  Anion in  $(\text{K-Crypt})_2$

Bi<sub>2</sub> on the Basis of Relativistic Electronic Structure Calculations. *J. Phys. Chem. A* **2005**, *109*, 1675–1683.

(60) Armbrüster, M.; Schnelle, W.; Schwarz, U.; Grin, Y. Chemical Bonding in TiSb<sub>2</sub> And VSb<sub>2</sub>: A Quantum Chemical and Experimental Study. *Inorg. Chem.* **2007**, *46*, 6319–6328.

(61) Tremel, W.; Hoffmann, R. Square Nets of Main Group Elements in Solid-State Materials. *J. Am. Chem. Soc.* **1987**, *109*, 124–140.

(62) Landrum, G.; Dronskowski, R. The Orbital Origins of Magnetism: From Atoms to Molecules to Ferromagnetic Alloys. *Angew. Chem., Int. Ed.* **2000**, *39*, 1560–1585.

(63) Amsler, M.; Naghavi, S. S.; Wolverton, C. Prediction of Superconducting Iron-Bismuth Intermetallic Compounds at High Pressure. *Chem. Sci.* **2017**, *8*, 2226–2234.